The kinetic energy of lithium-7 above and below the martensitic transformation

1994 J. Phys.: Condens. Matter 6 4197

(http://iopscience.iop.org/0953-8984/6/22/018)

J. Phys.: Condens. Matter 6 (1994) 4197–4212. Printed in the UK

The kinetic energy of lithium-7 above and below the martensitic transformation

A C Evans†§, J Mayers‡ and D N Timms†

† Physics Department, University of Portsmouth, Park Building, Portsmouth PO1 2DZ, UK
‡ Rutherford Appleton Laboratory, ISIS Facility, Chilton, Oxfordshire OX11 0QY, UK

Received 11 February 1994

Abstract. The atomic momentum distribution of lithium-7 in natural Li has been determined as a function of temperature from 20 to 300 K. The experiments were undertaken within the impulse approximation using the electronvolt spectrometer at ISIS. Final state effects were present above the statistical accuracy of our data and were accounted for by symmetrizing the neutron Compton profiles. The mean atomic kinetic energy of the Li nucleus was obtained directly from our measurements and was found to be $\sim$ 10% higher than that predicted by a harmonic model incorporating a density of states derived from previous phonon measurements. A fit of the data to the Debye model gave a Debye temperature of 419 ± 3 K.

1. Introduction

Neutron Compton scattering (NCS) or deep inelastic neutron scattering (DINS) is a recently developed technique that provides a direct measurement of the mean atomic kinetic energy of the scattering nucleus. The technique is only possible due to the intense flux of electronvolt neutrons available at pulsed neutron sources and is not feasible with conventional reactor based sources. Atomic kinetic energies can be determined from the phonon dispersion curves measured in inelastic neutron scattering experiments or from x-ray Debye–Waller factors; however, Peek *et al* [1] have pointed out that the values obtained may to some extent depend on the interpretation method used. The NCS technique has already proved successful in determining atomic momentum distributions and in obtaining directly values for the mean kinetic energies of a number of the light elements, for example, hydrogen, graphite [2, 3], helium [4] and solid and liquid neon [1, 5–7]. In many ways NCS is analogous to photon Compton scattering, which has already been used to study the electronic states of valence electrons in metallic Li [8]. Both techniques operate within the regime of validity of the impulse approximation (IA), the approach to which has recently been investigated in liquid Li at 473 K by inelastic neutron scattering at momentum transfers in the range 19.0–29.3 Å^{-1} [9].

At normal pressure and room temperature Li exists with a BCC structure, but upon cooling below 78 K, it undergoes a martensitic structural phase transformation into a new allotrope [10]. Neutron scattering experiments have revealed that below 75 K metallic Li is a combination of a substantial fraction of the untransformed BCC phase and a rhombohedral 9R related (Sm type) structure coexisting uniformly throughout the material [11–20]. A partial transition from the 9R structure to an FCC structure under conditions of increased

§ Present address: Rutherford Appleton Laboratory, ISIS Facility, Chilton, Oxfordshire OX11 0QY, UK.

0953-8984/94/224197+16$19.50

pressure has been observed in high-resolution neutron diffraction experiments [14]. The FCC structure can also be obtained by cold working at low temperatures [21]. Theoretical total energy calculations [22] of several Li structures (HCP, FCC, BCC and 9R) have confirmed that the 9R phase is favoured at low temperatures and much interest has centred on the observed absence of superconductivity down to temperatures of 6 mK [23].

There have been many measurements of various physical parameters for Li (see [24] for a review). Calculations of lattice specific heat and elastic constants for the BCC, FCC and 9R phases of Li have been made using a first-principles pseudopotential model [25] and the density and bulk and linear expansion coefficients have been derived from recent measurements [24]. The ground state electronic properties of Li have recently been calculated by quantum Monte Carlo methods [26]. The lattice dynamics of Li at low temperatures have been investigated by Wang and Overhauser [27], who calculated the phonon spectrum of the 9R phase from a pseudopotential model that fits the experimental BCC phonon spectrum at 98 K and compared their results with available experimental data.

An earlier study of Li at room temperature has been reported in [28]; however, these data were of rather poor statistical quality. In the present study we investigate the temperature dependence of the atomic momentum distribution of ^{7}Li in natural Li between 20 K and 290 K. The practical problems associated with obtaining the mean kinetic energy from the measured spectra are discussed and the results compared with values determined from available density of states data.

2. Recoil scattering

The interpretation of the spectra recorded in NCS experiments is based upon the impulse approximation (IA). Sears [29, 30] and Weinstein and Negele [31] have demonstrated that for a smooth scattering potential, the IA is reached asymptotically as the momentum transfer, q, tends to infinity. Inaccuracies in the momentum distribution measured by NCS are $\sim p/q$ [32] where p is the RMS atomic momentum and q the momentum transfer. Previous measurements suggest that this estimate is accurate to within a factor of approximately two [6]. Thus we would expect that for Li with a p value of 4–7 Å^{-1} momentum transfers of ~ 100 Å^{-1} are required to reduce inaccuracies to the $\sim 5\%$ level. Such large values of q are only available at pulsed neutron sources such as the ISIS facility at the Rutherford Appleton Laboratory.

Within the IA, the measured neutron scattering function $S(q, \omega)$ is simply related to the ground state momentum density of the recoiling atoms $n(p)$ by the equation [33]

$$S(q,\omega) = \int n(p)\delta\left(\omega - \omega_R - \hbar^2 \frac{q \cdot p}{M}\right) \mathrm{d}p \tag{1}$$

where ω is the energy and q is the momentum transfer, $\omega_R = \hbar^2 q^2/2M$ is the recoil energy of the atom of atomic mass M and the δ-function restricts the integration to those states that are accessible with energy and momentum conservation. Choosing q along the z-axis of a Cartesian co-ordinate system gives

$$S(q,\omega) = (M/q)J(y) \tag{2}$$

where

$$y = (M/q)(\omega - q^2/2M) \tag{3}$$

and

$$J(y) = \iint n(p_x, p_y, p_z)\,\mathrm{d}p_x\,\mathrm{d}p_y. \tag{4}$$

The quantity $J(y)$ is often termed the 'neutron Compton profile' and is the one-dimensional projection of the atomic momentum distribution along the direction of the scattering vector. Deviations of the dynamical structure factor from that given by equation (1) occur at finite values of momentum transfer. These effects are known generically as 'final state effects' (FSEs) [34, 35], although initial state effects are also important [32]. FSEs introduce asymmetry into $J(y)$ and shift its centroid to negative momenta. It is important to assess the significance of FSEs when deducing kinetic energies from the measured $J(y)$. For an isotropic harmonic system $S(q < \omega)$ can be calculated exactly [36] and programs have been written to simulate electronvolt spectrometer (EVS) data using this model. In section 5 we compare simulations with data collected from Li.

It can be shown that for a harmonically bound solid $J(y)$ becomes a Gaussian of energy width σ_y centred on the recoil energy,

$$J(y) = \left(1/\sqrt{2\pi\sigma_y^2}\right)\exp(-y^2/2\sigma_y^2) \tag{5}$$

where σ_y is related to the mean atomic kinetic energy E_K via

$$E_K = \tfrac{3}{2}\sigma_y^2/M. \tag{6}$$

Thus, by fitting a Gaussian convolved with the instrumental resolution function to the measured $J(y)$, we obtain a direct measurement of the mean atomic kinetic energy.

3. Measurements

The measurements reported here were performed using the EVS at the ISIS facility, which is situated at the Rutherford Appleton Laboratory. The EVS is an inverse geometry instrument, which uses a foil with a strong cross-section for neutron absorption to define the scattered neutron energy. A brief description of the experimental arrangement is given here. Full details of the EVS can be found elsewhere [37].

A white epithermal neutron beam was incident on a slab of natural Li of dimensions 50 mm × 50 mm × 3 mm thick. The sample was loaded in an open aluminium frame, mounted on an Al rod and suspended centrally in the beam inside the EVS sample tank with the plane of the sample perpendicular to the incident neutron beam. Care was taken to avoid hydrogenation of the sample and to ensure that no part of the sample holder was viewed by the incident neutron beam, which has dimensions 30 mm × 30 mm at the sample position. Both the sample tank and beamline were evacuated.

The scattered neutrons were detected in six banks of ^{3}He gas detectors, which were arranged in pairs symmetrically about the incident beam (see figure 1). The incident and transmitted neutron intensities were monitored using glass scintillation counters positioned in the evacuated beamline before and after the sample. The EVS detectors covered scattering angles in the ranges 35–53°, 57–76° and 125–137°. Forty detectors are arranged in the forward-scattering angles ($\theta < 90°$) and a further ten at back scattering. The lowest-angle detector bank is best suited for the study of hydrogenous systems for which the dynamics of the interaction restricts the scattering to $\theta < 90°$. The resolution of EVS is a complicated

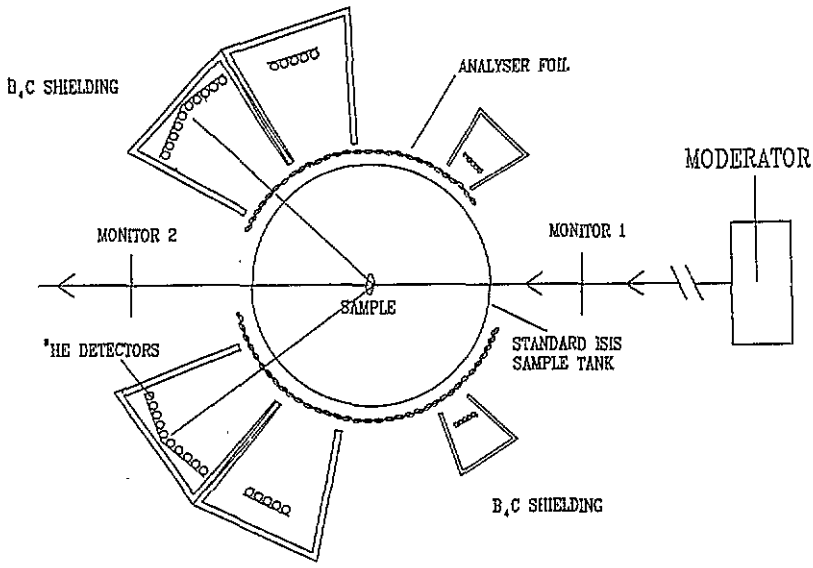

Figure 1. The electronvolt spectrometer. Pulses of neutrons with a wide range of energies arrive from the moderator. Neutrons scattered into a specific energy, defined by resonant foils around the sample, are detected by fifty ^{3}He neutron detectors arranged symmetrically about the incident beam direction. The detectors are arranged in three banks covering scattering angles in the ranges 35–53°, 57–76° and 125–137°. The ten detectors at back-scattering and the twenty detectors at intermediate-scattering angles were used for this study.

function of the atomic mass of the scatterer and the spectrometer geometry [38,39]. For recoil scattering from Li the resolution is significantly better at larger scattering angles and only the ten ^{3}He detectors at back-scattering and twenty detectors at intermediate-scattering angles were used in the data analysis.

Gold foils were mounted on a cylindrical Al support and placed between the sample and the ^{3}He gas detectors (see figure 1). The time of flight (TOF) spectra of scattered neutron were recorded both with and without the foil in the scattered neutron beam. The foils were automatically cycled in and out of the scattered beam every 5 min by means of pneumatic pistons. The constant cycling of the resonant foils in and out of the scattered beam was necessary to minimize the effects of drift in the relative efficiency of the detectors. The 'foil in' and 'foil out' data were automatically recorded and updated for every foil change. The Au foil has a strong absorption cross-section of Lorentzian shape, centred at 4922 meV and with an HWHM of 140 meV. By taking the difference between spectra collected with 'foil in' and 'foil out' we determine the count rate for neutrons scattered with energy 4922 ± 140 meV.

Data were collected for a total of 5 h at each of twenty-one temperatures in the range 20–300 K. Diffraction and DINS data are recorded simultaneously on the EVS. The recorded TOF regions of these data are very different (DINS, 100–700 μs; diffraction; 1000–20 000 μs) and so it was possible to monitor structural changes whilst measuring $J(y)$.

4. Data analysis

The data analysis procedures for the EVS are described fully elsewhere [6,37], but some of the more salient points are repeated here. The 'foil out' and 'foil in' TOF spectra for each

detector in turn were suitably normalized and then subtracted. Figure 2 shows a typical differenced TOF spectrum obtained from one detector at a scattering angle of 139.8°. Two features are visible in the figure. The more significant peak at 260–320 μs corresponds to the superposition of spectra of recoil scattering from the ^{6}Li and ^{7}Li nuclei in the sample. The smaller feature at 320–360 μs is the result of recoil scattering from Al in the thermal shield surrounding the sample. The Al scattering was determined by a separate measurement performed without the Li sample in place and the resulting TOF spectra were subtracted from each corresponding data set.

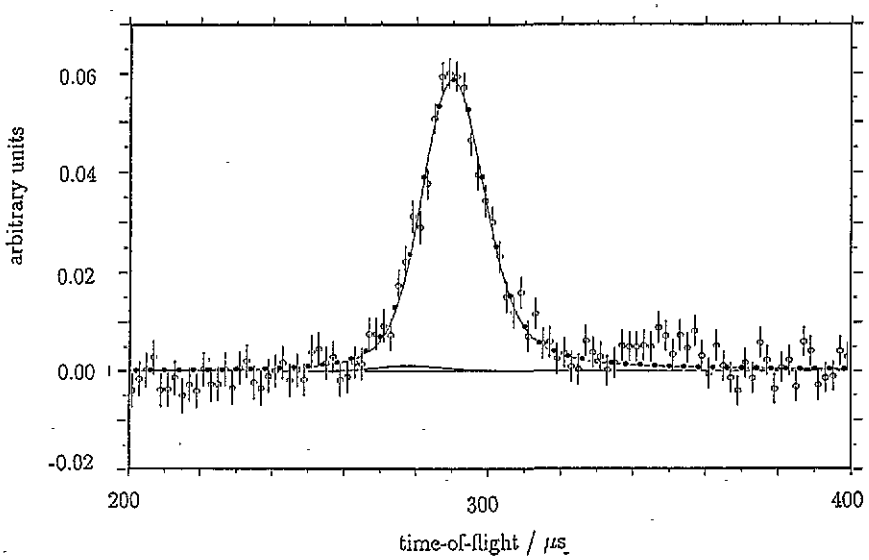

Figure 2. A typical TOF spectrum obtained from one ^{3}He gas detector. The scattering angle was 139.8°. The data display a feature at 260–320 μs corresponding to the superposition of ^{6}Li and ^{7}Li scattering. The small feature from 320 to 360 μs is the recoil scattering from the Al sample holder. The ^{6}Li and ^{7}Li scattering contributions are represented by the solid line. The solid circles are the difference between these two.

It was necessary to model the scattering in TOF to remove the ^{6}Li scattering contribution. This calculation requires the relative scattering powers of the two isotopes, which is the ratio of the product of the isotopic abundance and scattering power of each isotope. The isotopic abundances of ^{6}Li and ^{7}Li are 7.52% and 92.48% respectively and the total neutron scattering cross-sections are 0.98 and 1.44 barns respectively. Therefore the ratio of the relative scattering powers of ^{6}Li to ^{7}Li is 0.055:1. A least-squares fit in TOF was made to the Li recoil peaks using the following expression for the measured spectra:

$$S(t) = R(t) \otimes (aG(t - t_{r7}) + bG(t - t_{r6}))A \tag{7}$$

where A is a scaling factor, $\otimes$ signifies a convolution, $R(t)$ is the instrument resolution function, $a : b = 1 : 0.055$, $G(t - t_r)$ is a Gaussian centred at the IA recoil position $t = t_r$, and t_{r6} and t_{r7} are the recoil peak positions for ^{6}Li and ^{7}Li. Assuming that the binding forces of ^{6}Li and ^{7}Li atoms are identical and harmonic, we fix the ratio of the widths of the two isotopic peaks at $(\frac{6}{7})^{1/4}$. The ^{6}Li Gaussian and the sum of the two fitted Gaussians

are shown in figure 2. The fitted contribution from ^{6}Li scattering was removed and the resulting ^{7}Li spectrum from each detector was transformed into y-space using equation (3).

In order to deduce the width σ of each $J(y)$ and hence the kinetic energy of the ^{7}Li nucleus, the resolution function in y-space of each detector must be known. Analytical expressions for the components of the instrument resolution are given in a previous paper [38]. There are five independent contributions to the resolution in y-space, which originate from uncertainties in the measured TOF and in the distribution of the initial (L_0) and final (L_1) flight paths, scattering angles and incident energy values allowed by the instrument geometry and analyser foil resolution. The dominant contribution is from the intrinsic energy width of the Au resonance used. This function was previously determined for each detector, both analytically [37, 40] and experimentally by measurements of recoil scattering from heavy systems such as Pb or Sn, and is well described by a Lorentzian function. The angular resolution contribution is small, and was determined for all detectors from the line shape of powder diffraction peaks. Uncertainties in L_0 result from the depth of the moderator [37]; however, for a low-mass system such as Li, the contribution to the resolution from uncertainties in both L_0 and L_1 is small compared to the energy width of the resonant foil. The uncertainty in the TOF, Δt, is mainly due to time jitter in the electronics and is the second largest contribution to the resolution width. All resolution components except that from the Lorentzian resonance are well described by Gaussian functions. The resultant resolution function is therefore a Voigt function, i.e. a convolution of a Lorentzian and a Gaussian. Values of the different resolution components for the detectors at scattering angles of 133.2° and 67.2° are listed in table 1. These detectors were situated at the centre of the two banks used in this study. These data show that in each case the dominant contribution arises from the Au resonance and that the back-scattering bank can offer data with a resolution up to 50% better than that available with detectors in the intermediate bank.

The mean atomic kinetic energy was determined by fitting each individual momentum space differenced spectrum with a Gaussian, of the form given by equation (8) below, convoluted with the appropriate resolution function.

$$J(y) = \left(1/\sqrt{2\pi\sigma_y^2}\right) \exp(-(y - y_m)^2/2\sigma_y^2). \tag{8}$$

The two fitting parameters were σ_y and the profile centroid, y_m. The value of σ_y determines the mean atomic kinetic energy and deviations of y_m from zero can given information regarding the significance of FESs and the validity of the IA. Values for σ_y were determined at each temperature for each spectrum and then averaged to give a single value at each temperature for all detectors in each bank.

5. Experimental results and simulations

The diffraction data collected at 300 K with the back-scattering bank are shown in figure 3(A) after conversion to d-spacings. Using the data given in [14] it was possible to assign all peaks in figure 3(A) to BCC Li, thus demonstrating that the sample had not become exposed to moisture at any time. In fact the presence of hydrogen in the form of lithium hydride would have appeared as a broad recoil peak in the spectra recorded with the forward-scattering detectors: no such peak was observed. Figure 3(B) shows the diffraction spectra of Li at 22.6 K. Additional peaks have appeared, which can largely be attributed to the 9R phase. The BCC phase is still present, as can be seen by comparing figures 3(A) and 3(B)

Table 1. Values of the different resolution components for detectors situated at the centre of the back and intermediate detector banks.

	L_0	L_1	θ	t	E_1
Parameter value	11.055(0.01) m	0.494(0.005) m	133.18(0.20)°	-6.3(0.2) μs	4922(10) meV
Resolution width (meV)	0.020(0.005)	0.009(0.001)	1.04(0.02)	1.45(0.05)	139(4)
y resolution at back-scattering $(Å)^{-1}$	0.379	0.215	0.444	1.063	3.123
y resolution at intermediate-scattering $(Å)^{-1}$	0.580	0.285	0.480	1.405	4.879

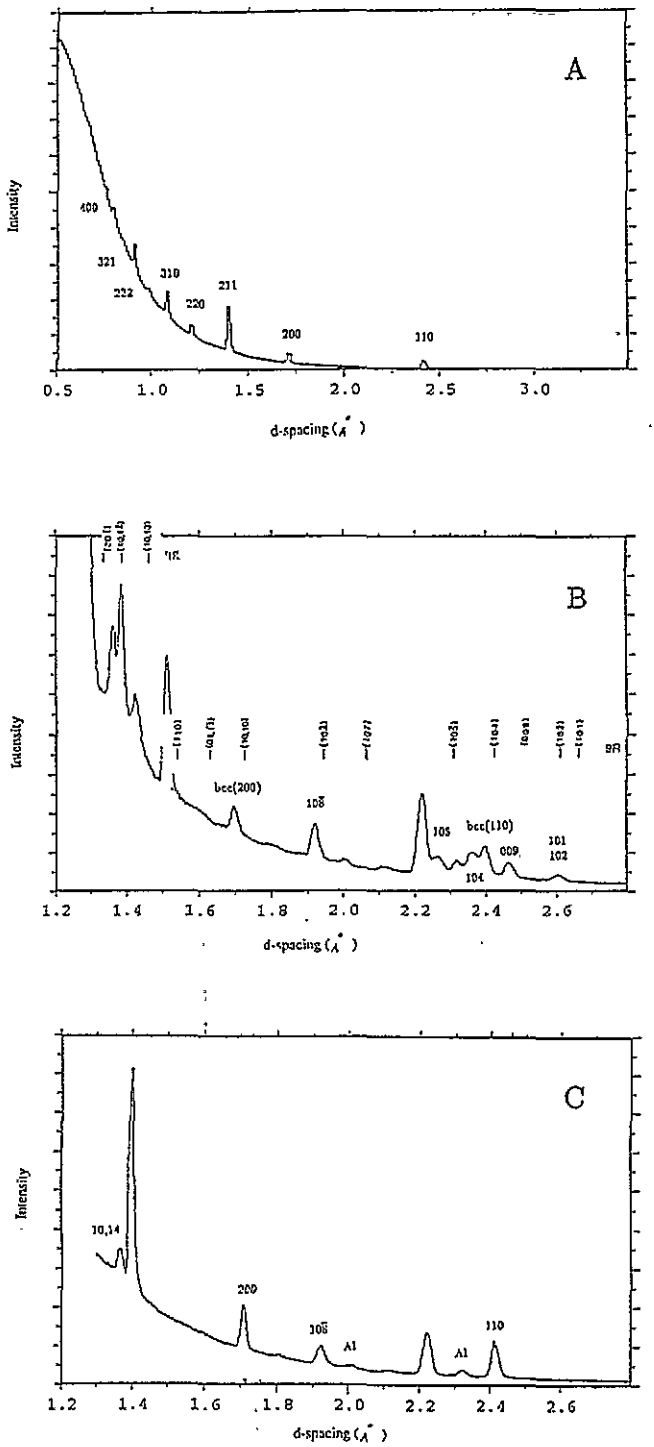

Figure 3. Diffraction data recorded with the ten back-scattering detectors at (A) 300 K, (B) 22.6 K and (C) 120 K. At 300 K all peaks are assigned to BCC Li. At 22.6 K additional peaks have appeared, which can be attributed to the 9R phase. Upon warming to 120 K, a small amount of the 9R phase is frozen in.

and Al peaks are also visible. This time the Li peaks are labelled using the values at 20 K quoted in [15]. The difference between the EVS results and the ideal peak positions can be attributed to the presence of stacking faults. It is known that stacking faults in the 9R structure broaden and cause deviations of the (h, k, l), $l \neq 0$ diffraction peaks from their ideal values [13], making the indexing of the 9R peaks difficult as the peaks are shifted by different amounts. Nevertheless, in figure 3(B) the peaks are marked with the index considered most likely. It has been found in previous studies that a Rietveld refinement is not possible in the 9R phase. Upon warming to 120 K, most of the 9R peaks diminish but do not entirely disappear (see figure 3(C)). Surprisingly, a small portion of the 9R related phase remained present in all subsequent measurements made at temperatures above the predicted martensitic transition temperature.

No discontinuity in the temperature variation of the kinetic energy was observed in the region of the martensitic phase transition. This is not surprising because the transition gives rise to only a small change in mean atomic separation ($\sim 0.01\%$) which is unlikely to give rise to a change in the mean kinetic energy observable at the present statistical accuracy of these data. In addition, the presence of the 9R phase above the transition temperature would have diluted any observable effect.

Figure 4 shows momentum space data collected with the back-scattering detector bank at temperatures of 22.6 and 260.5 K. For an isotropic system each detector measures an independent neutron Compton profile and each data set shown is the weighted sum, normalized to unity, of the data collected in each of the ten detectors in this bank. The weighting factors used were proportional to the detected intensity at a given scattering angle, which depends on the instrument geometry, detector efficiency and the angular distribution of the scattered intensity. The instrument resolution function is included as the solid line in figure 4 and is the same in each case. Hence the difference in the width of the two data sets is a direct consequence of the temperature change. It should be noted that each data set tends to the zero baseline at high momenta, thus demonstrating the low background present in these data.

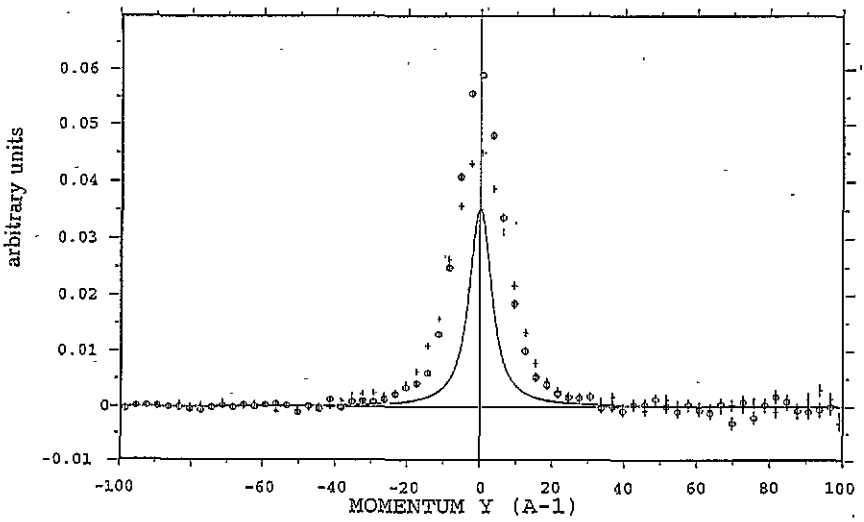

Figure 4. The neutron Compton profiles measured by the ten back-scattering detectors at temperatures of 22.6 K (circles) and 260.5 K (crosses). The resolution function is included as the solid line.

Table 2. The unsymmetrized and symmetrized experimental values of σ_y measured with both the intermediate (INT) and back-scattering (BS) detector banks. The corresponding kinetic energies (E_K) are also listed.

	Unsymmetrized				Symmetrized			
Temperature (K)	σ_y(BS) (Å)$^{-1}$	E_K(BS) (meV)	σ_y(INT) (Å)$^{-1}$	E_K(INT) (meV)	σ_y(BS) (Å)$^{-1}$	E_K(BS) (meV)	σ_y(INT) (Å)$^{-1}$	E_K(INT) (meV)
22.6	4.65(0.07)	6.46	4.76(0.10)	6.77	4.74(0.05)	6.71	5.01(0.07)	7.49
25.5	4.75(0.07)	6.74	4.95(0.10)	7.32	4.80(0.05)	6.88	5.22(0.07)	8.14
33.0	4.69(0.07)	6.57	4.88(0.10)	7.11	4.77(0.05)	6.79	5.16(0.07)	7.95
40.5	4.61(0.07)	6.32	4.93(0.10)	7.26	4.70(0.05)	6.60	5.21(0.07)	8.11
50.7	4.68(0.07)	6.54	4.92(0.09)	7.23	4.78(0.05)	6.82	5.11(0.06)	7.80
60.6	4.71(0.08)	6.62	4.79(0.12)	6.85	4.79(0.06)	6.85	5.04(0.08)	7.58
60.8	4.61(0.07)	6.35	4.94(0.10)	7.29	4.68(0.05)	6.54	5.18(0.07)	8.01
69.5	4.80(0.08)	6.88	5.01(0.10)	7.49	4.91(0.05)	7.20	5.26(0.07)	8.26
79.4	4.80(0.07)	6.88	4.92(0.10)	7.23	4.91(0.05)	7.20	5.16(0.07)	7.94
88.2	4.76(0.07)	6.77	5.41(0.10)	8.74	4.87(0.05)	7.08	—	—
98.3	5.07(0.08)	7.68	5.03(0.10)	7.55	5.15(0.05)	7.92	5.33(0.07)	8.48
98.8	4.86(0.15)	7.05	5.07(0.21)	7.68	4.97(0.10)	7.38	5.19(0.14)	8.04
107.5	4.90(0.07)	7.17	5.15(0.10)	7.92	5.03(0.05)	7.55	5.46(0.07)	8.90
117.6	5.15(0.09)	7.92	5.27(0.13)	8.29	5.22(0.07)	8.14	5.69(0.09)	9.67
126.7	5.06(0.07)	7.65	5.14(0.10)	7.89	5.13(0.05)	7.86	5.45(0.07)	8.87
136.7	5.27(0.07)	8.29	5.60(0.12)	9.36	5.36(0.05)	8.58	5.57(0.07)	9.26
174.5	5.71(0.13)	9.74	5.75(0.18)	9.87	5.81(0.09)	10.08	6.03(0.11)	10.86
203.0	5.94(0.10)	10.54	—	—	6.00(0.07)	10.75	—	—
232.0	6.15(0.08)	11.29	6.51(0.11)	12.65	6.21(0.06)	11.51	6.77(0.07)	13.69
260.5	6.65(0.09)	12.77	6.84(0.11)	13.97	6.21(0.06)	11.51	7.02(0.08)	14.71
300.3	6.78(0.08)	13.73	6.78(0.11)	13.73	6.85(0.06)	14.01	7.06(0.08)	14.88

The experimental σ_y values for both detectors bank at various temperatures between 22.6 and 260.5 K are plotted in figure 5. These values are tabulated in table 2 together with the atomic kinetic energy determined using equation (6). The values from the ten back-scattering detectors are shown as circles, whilst values obtained from data collected with the detectors in the angular range 57–77° shown as boxes. Good agreement is observed between the σ_y values obtained from the two detector banks. This is a clear indication that the data analysis routines have been successful in extracting σ_y from the measured spectra. It also indicates that the correct form of the resolution function for both detector banks has been applied. The temperature dependence of σ_y calculated from a measurement of the density of states [41] at 293 K is shown as the solid line in figure 5, while a calculation using the Debye density of states with $\theta_D = 400$ K is shown as the dashed line. The values calculated and the corresponding kinetic energies are listed in table 3.

Table 3. The σ_y values obtained both from a measurement of the density of statea of Li at 293 K [38] and from the isotropic Debye model using a Debye temperature of 400 K. The corresponding kinetic energies are also listed.

Temperature (K)	σ_y (Å)$^{-1}$ experiment	Kinetic energy (meV)	σ_y (Å)$^{-1}$ Debye	Kinetic energy (meV)
22.6	4.47	5.97	4.64	6.43
25.5	4.47	5.97	4.64	6.43
33.0	4.47	5.97	4.64	6.43
40.5	4.48	5.99	4.75	6.46
50.7	4.50	6.05	4.67	6.51
60.6	4.54	6.15	4.70	6.60
60.8	4.54	6.15	4.70	6.60
69.5	4.58	6.26	4.73	6.68
79.4	4.64	6.43	4.78	6.82
88.2	4.70	6.60	4.83	6.97
98.3	4.78	6.82	4.90	7.17
98.8	4.78	6.82	4.91	7.20
107.5	4.85	7.02	4.97	7.38
117.6	4.94	7.29	5.05	7.61
126.7	5.03	7.55	5.13	7.86
136.7	5.12	7.86	5.23	8.17
174.5	5.52	9.10	5.59	9.33
203.0	5.82	10.11	5.88	10.32
232.0	6.12	11.18	6.18	11.40
260.5	6.42	12.31	6.36	12.46

The exact simulations of the measured neutron Compton profiles of Li were performed by calculating the scattering function $S(q, \omega)$, for an isotropic harmonic solid using a Debye density of states with $\theta_D = 400$ K (see [32]). The simulated TOF spectra were convolved with the resolution function for each detector and converted to momentum space, then analysed in the same way as the 'real' EVS data. Extracting σ_y as a function of temperature, evaluating the Debye temperature and comparing with that used to simulate $S(q, \omega)$ provides a check on the success of the analysis routines in extracting the correct variance of $J(y)$ and on the validity of the IA. Figure 6 shows the weighted averages of data collected by detectors in the back-scattering bank. The measurement was performed at 260.5 K and the simulation for this temperature is shown as the solid line. Both the simulated and experimental profiles are slightly asymmetric. However, despite this deviation from a Voigt

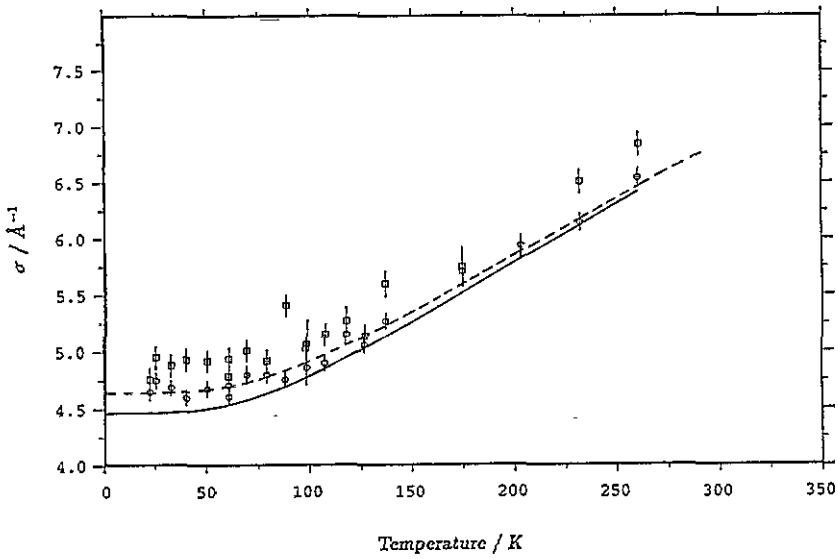

Figure 5. The temperature dependence of σ_y measured with the back-scattering bank (circles) and the intermediate bank (boxes). Good agreement is observed between the experimental data obtained with the two detector banks. The temperature dependence of σ_y calculated from a measurement of the density of states [41], and that calculated from the isotropic Debye model with a Debye temperature of 400 K, are shown as the solid and dashed lines respectively.

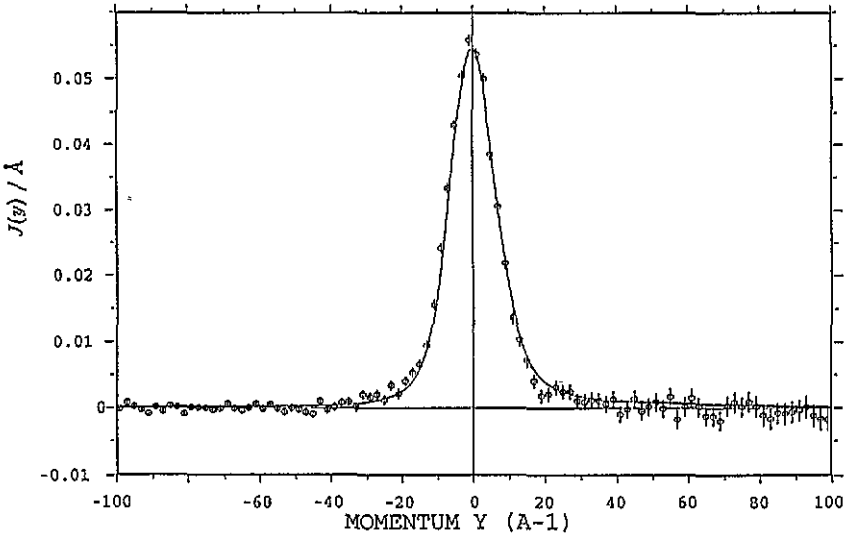

Figure 6. The simulated (solid line) and measured (circles) EVS data at 260.5 K.

function, the analysis routines extract σ_y values very close to that given by the Debye model used for the simulation. This is typical of all spectra.

The asymmetry of $J(y)$ indicates the presence of FSEs. In the IA, the recoil peak is centred about $y = 0$. This is asymptotically reached as the momentum transfer, $q \rightarrow \infty$. At

finite q the recoil peak is shifted to negative momenta and this shift becomes more negative at smaller q. This trend is observed in figure 7, where the fitted recoil peak position, Δy, for the measurement at 98.3 K is plotted as a function of momentum transfer. Also shown is the fitted recoil peak position for the exact simulation at 100 K from the measured density of states. The observed shifts are $\sim \sigma_y/y$ as predicted by theory. For example at a mean momentum transfer of 50 Å^{-1}, $\sigma_y/y \sim 10\%$ whereas the peak shift is $\sim 5\%$. This discrepancy is not unreasonable taking into account the errors associated with the location of the peak position and bearing in mind that σ_y/y is only an approximation. Sears [42] has shown that a series expansion in $J(y)$ has terms alternately symmetric and antisymmetric about $y = 0$. He showed that terms of order q^{-1} are antisymmetric and those of order q^{-2} are symmetric. Symmetrizing $J(y)$ about $y = 0$ cancels out all terms of order q^{-2} [6], leaving residual FSEs of order q^{-2}. All neutron Compton profiles were symmetrized and values for the variance of each profile were determined in the usual way. These values and the corresponding kinetic energies are also listed in table 2. Figure 8 compares the symmetrized and unsymmetrized data obtained with the back-scattering bank. The solid lines are single-parameter fits to the data using a Debye model with the Debye temperature, θ_D, as the fitting parameter. Values of 419 ± 2.7 K and 401.3 ± 3.7 K were obtained for the symmetrized and unsymmetrized data respectively. This figure demonstrates that FSEs are significant at a level above the statistical accuracy of these data.

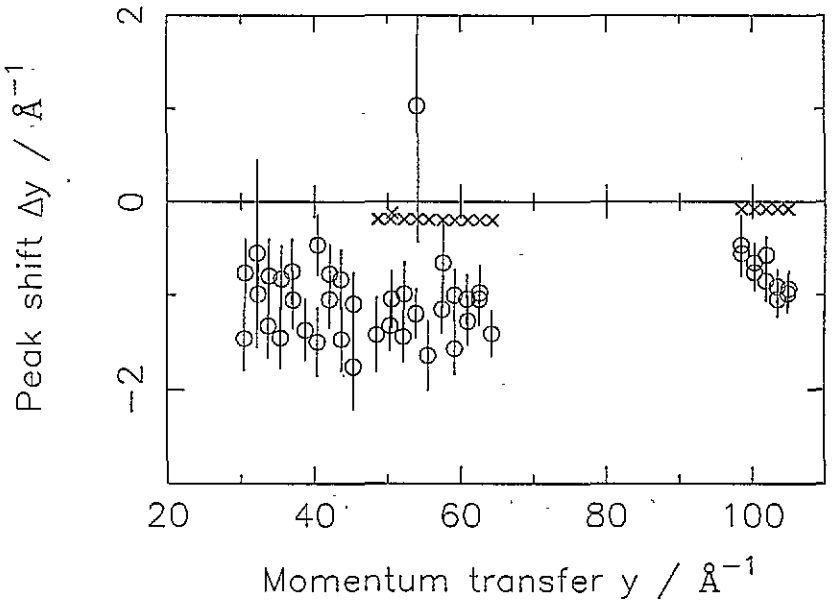

Figure 7. FESs are manifested as a shift in recoil peak from $y = 0$. This trend is observed here where the peak shift Δy (circles) is plotted as a function of momentum transfer for the measurement at 98.3 K. Also shown are the fitted peak positions to the exact simulation at 100 K from a measurement of the phonon density of states.

Li is a light atom with relatively weak binding and a large zero point motion. Since the harmonic approximation is based on an expansion of the potential for small r, it might be expected that Li would exhibit some anharmonicity. A previous NCS measurement [28]

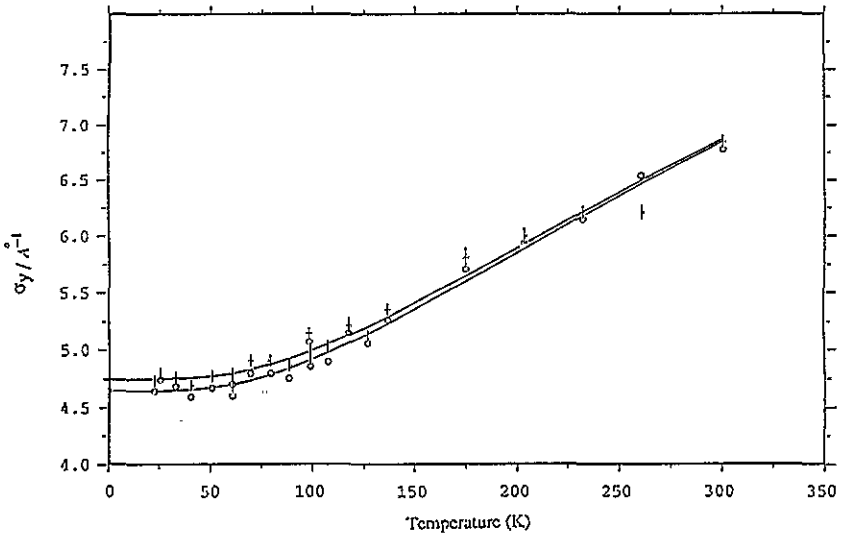

Figure 8. FSEs can be reduced by symmetrization of the data [43]. The symmetrized and unsymmetrized data for the back-scattering bank are shown as the crosses and circles respectively. The solid lines correspond to fits to the data using a Debye model.

reports figures for the kinetic energy of Li of $\sigma = 20 \pm 1.9$ Å^{-1} (with an Au analyser foil) at room temperature, which is some 40% larger than that obtained here. Comparing our symmetrized results to the density of states calculation we find that below 100 K, where the atomic kinetic energy is almost entirely due to zero-point motion, we obtain measured values which are consistently $10 \pm 2\%$ higher than the calculated values. An estimate of the size of the anharmonicity necessary to account for the observed discrepancy can be found by treating Li as an Einstein solid with N oscillators of frequency ω. First-order perturbation theory was applied to calculate the perturbed momentum distribution of ^{7}Li, assuming an anharmonic potential of the form

$$V(x) = \tfrac{1}{2}M\omega^2x^2 + \varepsilon(x/l)^4 \tag{9}$$

where $l - \sqrt{h/M\omega}$ and h is Planck's constant. The calculation of the perturbation is given in full in appendix 1 of [40]. It was found that a perturbation of the order of $\varepsilon = 0.05\ h\omega$ (where ω is the vibrational frequency of the ground state of the oscillator) was required in order to perturb the kinetic energy by 10%. Figure 9 shows the kinetic energy calculated from the density of states given in [41] plotted with the symmetrized back-scattering data.

6. Conclusions

From this work we can conclude that the mean atomic kinetic energy of the ^{7}Li nuclei in natural Li is $\sim 10\%$ higher than predicted by a harmonic model derived from a measurement of the density of states. This is in contrast to an earlier measurement in which the measured kinetic energies were some 40% larger than those reported here. Good agreement between data obtained from different detector banks and between the kinetic energies extracted from both the measured and simulated profiles emphasizes both the consistency of our data and the accuracy of the analysis procedures. FSEs are present in these data despite

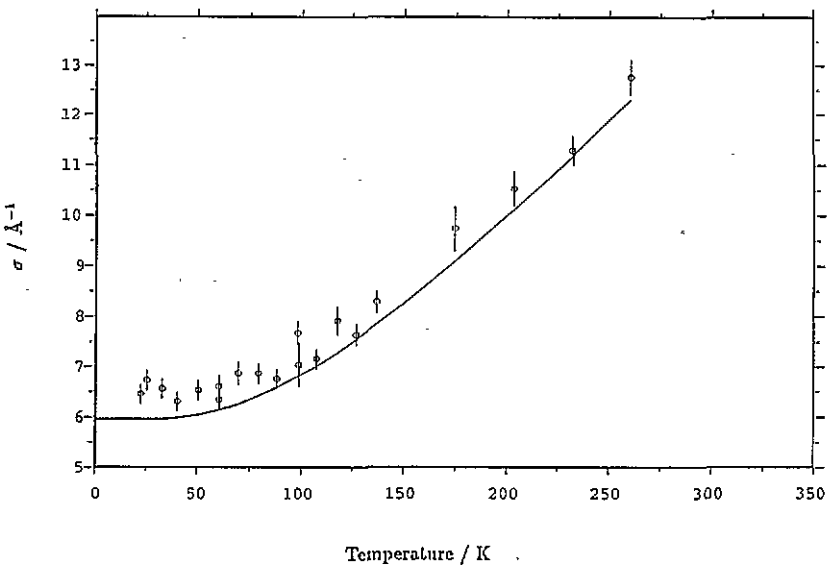

Figure 9. The symmetrized back scattering data are plotted together with the kinetic energy calculated from the density of states given in [41].

the high momentum transfers used and the recoil peaks are shited to negative momenta by amounts comparable to that predicted by theory. The symmetrization procedure of Sears [42] has been used to account for the FSEs and this results in a small increase in the extracted kinetic energies. Changes in the kinetic energy as a consequence of the martensitic transformation were not detected and the ability of the instrument to simultaneously record NCS and diffraction data facilitates the tentative explanation given.

Acknowledgments

We are grateful to the SERC for the provision of beam time and research support at the spallation neutron source at the Rutherford Appleton Laboratory. One of us (ACE) acknowledges the support of an SERC studentship.

References

[1] Peek D A, Fujita I, Schmidt M C and Simmons R O 1992 *Phys. Rev.* B **45** 9680
[2] Rauh H and Watanabe N 1984 *Phys. Lett.* **100A** 244
[3] Paoli M P and Holt R S 1988 *J. Phys. C: Solid State Phys.* **21** 3633
[4] Holt R S, Needham L M and Paoli M P 1987 *Phys. Lett.* **126** 373
[5] Peek D A, Schmidt M C, Fujita I and Simmons R O 1992 *Phys. Rev.* B **45** 9671
[6] Mayers J, Burke T M and Newport R J 1994 *J. Phys.: Condens. Matter* **6** 641
[7] Mayers J 1993 *Phys. Rev. Lett.* **71** 1553
[8] Cooper M J, Williams B G, Borland R E and Cooper J R A 1970 *Phil. Mag.* **22** 441
[9] Verkerk P, de Jong P H K, Arai M, Bennington S M, Howells W S and Taylor A D 1992 *Physica* B **180 & 181** 834
[10] Barret C S and Trautz O R 1948 *Trans. Am. Inst. Min. Metall. Pet. Eng.* **175** 57
[11] McCarthy C M, Tompson C W and Wrner C A 1980 *Phys. Rev.* B **22** 574

[12] Overhauser A W 1984 *Phys. Rev. Lett.* **53** 64
[13] Berliner R and Werner S A 1986 *Phys. Rev.* B **34** 3586
[14] Smith H G, Berliner R and Jorgensen J D 1989 *Physica* B **156 & 157** 53
[15] Berliner R, Fajen O, Smith H G and Hitterman R L 1989 *Phys. Rev.* B **40** 18
[16] Smith H G, Berliner R, Jorgensen J D, Nielsen M and Trivisonno J 1990 *Phys. Rev.* B **41** 1231
[17] Ernst G, Artner C, Blaschko O and Krexner G 1986 *Phys. Rev.* B **33** 6465
[18] Smith H G 1987 *Phys. Rev. Lett.* **58** 1228
[19] Smith H G, Dolling G, Nicklow R M, Vijayaraghavan P R and Wilkinson M K 1968 *Neutron Inelastic Scattering* vol 1 (Vienna: IAEA) p 149
[20] Schwarz W and Blaschko O 1992 *Physica* B **180 & 181** 271
[21] Barret C S 1956 *Acta Crystallogr.* **9** 671
[22] Zdetsis A D 1986 *Phys. Rev.* B **34** 7666
[23] Liu A Y and Cohen M L 1991 *Phys. Rev.* B **44** 9678
[24] Mel'nikova T N and Mozgovoi A G 1988 *High Temp.* **26** 6848
[25] Vazquez G J 1990 *Rev. Mex. Fis.* **36** 4572
[26] Sugiyama G, Zerah G and Alder B J 1989 *Physica* A **156** 144
[27] Wang Y R and Overhauser A W 1986 *Phys. Rev.* B **34** 8401
[28] Paoli M P 1988 *DPhil Thesis* University of Oxford
[29] Sears V F 1971 *Phys. Rev.* A **5** 452
[30] Sears V F 1973 *Phys. Rev.* A **7** 340
[31] Weinstein J J and Negele J W 1982 *Phys. Rev. Lett.* **49** 1016
[32] Mayers J 1990 *Phys. Rev.* B **41** 141
[33] Paoli M P and Holt R S 1988 *J. Phys. C: Solid State Phys.* **21** 3633
[34] Griffin A 1993 *Excitations in a Bose Liquid* (Cambridge: Cambridge University Press)
[35] Mayers J 1989 *Rutherford Appleton Laboratory Report* RAL-89-104
[36] Mayers J, Andreani C and Baciocco G 1989 *Phys. Rev.* B **39** 1016
[37] Mayers J and Evans A C 1991 *Rutherford Appleton Laboratory Report* RAL-91-048
[38] Andreani C, Baciocco G, Holt R S and Mayers J 1989 *Nucl. Instrum. Methods* A **276** 297
[39] Timms D N, Cooper M J, Holt R S and Postorino P 1990 *Nucl. Instrum. Methods* A **294** 509
[40] Evans A C 1993 *PhD Thesis* University of Warwick
[41] Beg M M and Nielsen M 1976 *Phys. Rev.* B **14** 4266
[42] Sears V F 1984 *Phys. Rev.* B **30** 44
[43] Martel P, Svensson E C, Woods A D B, Sears V F and Cowley R A 1976 *J. Low Temp. Phys.* **23** 285